14th International Symposium on Turbulence and Shear Flow Phenomena (TSFP14)
Heidelberg, Germany, July 28–31, 2026

OUTER-LAYER SIMILARITY AND INNER–OUTER INTERACTIONS IN PIPES WITH REGULAR SINUSOIDAL ROUGH WALLS

Siavash Toosi
Institute of Fluid Mechanics (LSTM)
Friedrich–Alexander–Universität (FAU)
Erlangen, Germany
siavash.toosi@fau.de

Daniele Massaro
Department of Mechanical Engineering
Massachusetts Institute of Technology (MIT)
Cambridge, MA, USA
danmas@mit.edu

Philipp Schlatter
Institute of Fluid Mechanics (LSTM)
Friedrich–Alexander–Universität (FAU)
Erlangen, Germany
philipp.schlatter@fau.de

ABSTRACT

Wall-bounded turbulent flows are often assumed to exhibit outer-layer similarity, where the outer-layer flow, when appropriately scaled, becomes independent of wall roughness. We assess this hypothesis using proper orthogonal decomposition (POD), which identifies the energetically-dominant coherent structures and provides a compact, objective basis for comparing flow organization between smooth and rough-walled flows. The analysis quantifies differences in the spatial shape of corresponding POD modes via the angle between them, based on their inner product. The POD is done on three-dimensional (3D) snapshots of the turbulent pipe flow at friction Reynolds number of $Re_\tau \approx 2000$, with roughness heights of 0, 10, and 20 in friction units (smooth, and rough with heights of 0.5% and 1% of the pipe radius), obtained using direct numerical simulation (DNS). Results show that the POD mode shape differences between rough and smooth pipes exceed thresholds attributable to computational factors (flow realization, sampling frequency, etc.) and variations in the friction Reynolds number. Moreover, the POD modes of rough-walled cases are more similar to each other than to the smooth pipe, suggesting that turbulent structures in the outer region may differ between smooth and rough pipes. Further studies are needed to confirm this.

SIMULATION SETUP

The simulation design of this work is inspired by the work of Chan et al. (2018), and extended to higher Reynolds numbers. Three friction Reynolds numbers of $Re_\tau \approx 550$, 1000, and 2000 are considered in the simulation campaign. The wall roughness has a functional form of

$$\delta r = h \cos\frac{2\pi z}{\lambda} \cos\frac{2\pi R\theta}{\lambda}, \qquad (1)$$

where δr is the roughness height, z and θ are streamwise and azimuthal coordinates of the wall, R denotes the pipe's radius, h is the roughness amplitude (or height), and λ is the roughness wavelength that is identical in the streamwise and azimuthal directions. Here, h is set in friction units (based on the friction length of the smooth pipe at the same bulk Reynolds number, $\delta_{\nu,s}$) and has values of $h^+ = h/\delta_{\nu,s} \approx 10$, 20, and 40. The wavelength λ is selected to have a constant λ/h ratio of 7.5 for $Re_\tau \approx 2000$. A smooth case was also simulated as a baseline for comparison. Both smooth and rough pipes have a length of $8\pi R$ in the streamwise direction. The simulation campaign involves a total of 12 cases with four setups per friction Reynolds number (only a subset of which is used here). The convention adopted here is as PR^+-h^+ where $R^+ = Re_{\tau,s} = R/\delta_{\nu,s}$ is the friction Reynolds number and h^+ is the roughness amplitude, such that P550-0 and P2000-20 correspond to a smooth pipe at $Re_\tau \approx 550$ and a rough pipe at $Re_{\tau,s} \approx 2000$ with $h^+ \approx 20$. Figure 1 illustrates the computational domain, including the shape of the walls, for P2000-40. A summary of the relevant cases used in this work is given in Table 1.

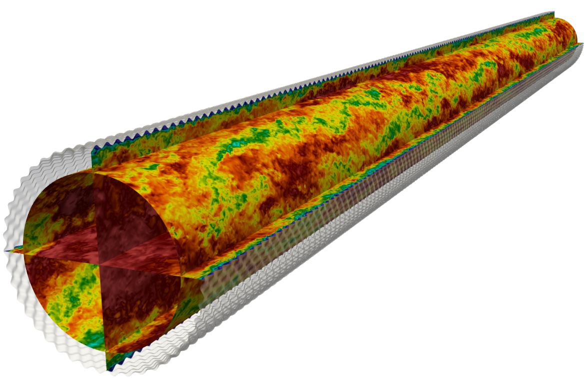

Figure 1: A schematic of the roughness shape and the flow inside the pipe for P2000-40. The gray transparent surface shows the wall, while the pseudocolor shows streamwise velocity from lowest (blue) to highest (red) values.

Table 1: A summary of the main simulation setups used here. Re_D, $Re_{\tau,s}$ and Re_τ are the bulk (based on diameter), friction Reynolds number in the corresponding smooth wall, and the actual friction Reynolds number, respectively. h and λ are the amplitude and wavelength of the cosine shaped roughness and R denotes the radius of the pipe.

Case	Re_D	$Re_{\tau,s}$	Re_τ	h^+	h/R	λ/h
P2000-0	83000	2000	1998	0	0	—
P2000-10	83000	2000	2422	10	0.005	7.5
P2000-20	83000	2000	2881	20	0.01	7.5
P2000-40	83000	2000	3346	40	0.02	7.5

We carried out direct numerical simulation (DNS), using the code Neko (Jansson et al., 2024) which is a spectral-element solver primarily designed for incompressible Navier–Stokes equations. The grids used in this work have resolutions of $(\Delta z^+, \Delta r^+, R^+\Delta\theta) = (\Delta z, \Delta r, R\Delta\theta)/\delta_{v,s} \approx (5.1, 0.3, 5.3)$ next to the wall for the rough pipes, and $(10, 0.5, 5.3)$ for the smooth ones. Transients are removed by discarding at least the first $300R/U_b$ (where U_b is the bulk velocity) time units on the final mesh, with statistics collected over the next $500R/U_b$ (around $24ETT$, where $ETT = R/\sqrt{\tau_{wall,s}/\rho}$ is the eddy turnover time based on the smooth pipe friction). Figure 2 shows the mean velocity and Reynolds stresses obtained for P2000-0, P2000-10, and P2000-20 (the three main flows studied here) at different streamwise and azimuthal locations along the sinusoidal roughness element. As expected, the mean profiles become independent of the spatial sampling location farther from the wall.

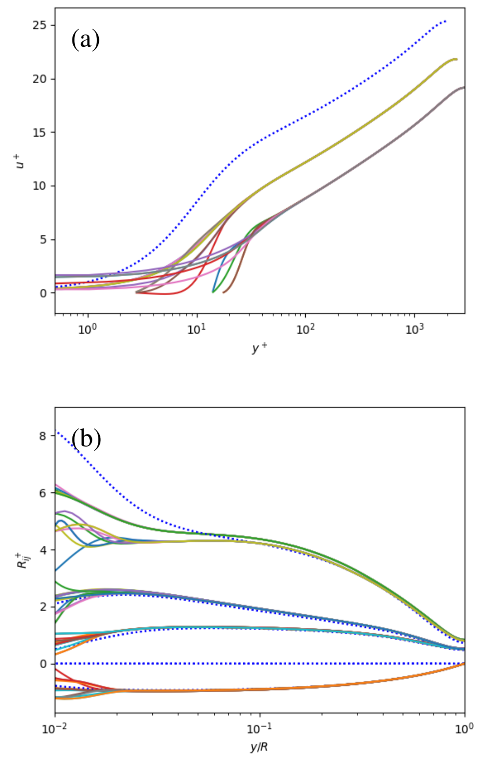

Figure 2: (a) Mean velocity and (b) Reynolds stresses (b) for P2000-10 and P2000-20 (solid lines) compared to P2000-0 reference data of Yao et al. (2024) at $Re_\tau \approx 2000$ (dotted blue lines). For each of the rough cases multiple streamwise and azimuthal locations are shown along the sine roughness pattern. The collapse of the lines imply an independence of the flow from wall roughness away from the wall. P2000-0 of this simulation campaign matches that of Yao et al. (2024) and is not shown here.

METHODOLOGY

The goal here is to modally decompose the flow (via POD) and assess the outer-layer similarity by comparing the respective POD modes between different flows. An advantage of using POD for this analysis is that the information from different radial (wall-normal) locations and velocity components are combined together in a quantitative manner. Another advantage is that the decomposition contains more information about the statistical structure of the flow, including spatial and temporal correlations. In addition, POD is mathematically well-understood, and robust to numerical aspects.

Proper Orthogonal Decomposition (POD)

For a flow with a statistically homogeneous spatial direction – thus a continuous translational symmetry – the POD modes converge to Fourier modes (cf. George, 1988). The spatial POD modes for velocity component i thus take the form,

$$\phi_{i,qk_\theta k_z} = f_q(r)\mathrm{e}^{i(k_\theta\theta + k_z z)},$$

where q is the quantum index in the radial direction, and k_θ and k_z are the Fourier wavenumbers in the azimuthal and streamwise directions.

In the presence of roughness, the POD modes only follow a discrete symmetry set by the roughness wavelengths. Since we are only interested in the outer region of the flow, and assuming that farther from the wall the symmetry becomes closer to a continuous one (note that this arguably has some potential overlap with the assumption of outer-layer similarity), we will use the same method (i.e., Fourier expansion) for the rough pipes as well. Note that only a region $r \leq R_{max}$ above the roughness peaks can be considered in the Fourier expansion and thus the POD.

Enforcing the translation symmetry, and therefore the Fourier expansion, results in a larger number of modes where each (radial) structure is potentially represented by multiple streamwise and azimuthal modes. This means that the energy contained within that structure is the sum of the energy of its constituting Fourier modes. This is a well-known issue in the field, related to symmetries (cf. Rowley and Marsden, 2000; Marensi et al., 2023). One possible approach to deal with this is employing a secondary classification method to identify Fourier modes that are related to the same structure, as done by, e.g., Massaro et al. (2024) using a Voronoi-based method. In this work, we adopt a mode-by-mode comparison between flows, which provides a direct generalization of two-dimensional energy spectra to the full 3D spatial structure.

Figure 3 illustrates the reduction of the 2D energy spectra at multiple radial locations to the energy spectrum of the total energy contained within each Fourier mode, and that contained within the first radial POD mode $q = 1$. We note that modes with longer wavelengths contain more of the total energy of the flow. Furthermore, for those longer wavelengths a larger portion of the energy is contained within the first POD mode. This can significantly simplify our analysis and reduce the question of outer-layer similarity to a comparison of the POD modes for the first few quantum indices.

Measurement of POD Mode Dissimilarity

The quantitative measure used here to assess the similarity of the POD modes is the angle between them, based on the same inner product used for obtaining the POD modes.

The inner product of two modes, $\phi_{i,qk_\theta k_z}(r)$ and $\phi'_{i,qk_\theta k_z}(r)$ (for the same k_θ and k_z) is defined using the dot product

$$\langle \phi, \phi' \rangle = \frac{1}{V_{tot}} \int_V \phi^* \phi' \mathrm{d}V = \frac{L_z}{V_{tot}} \int_A f_q^* f_q' \mathrm{d}A = \frac{L_z}{V_{tot}} \int_0^{r_{max}} f_q^* f_q' 2\pi r \mathrm{d}r,$$

where no summation over q is implied, $(\cdot)^*$ denotes the complex conjugate, L_z is the streamwise length of the computational domain, r_{max} is the outermost extent of the integration (farthest from the centerline), and $V_{tot} = \pi r_{max}^2 L_z$ is the total volume of the computational domain. Since POD modes are orthonormal, we have $\langle \phi, \phi \rangle = \langle \phi', \phi' \rangle = 1$ for same q, k_z, and k_θ.

The idea here is to use the dot product to quantify the similarity of modes ϕ and ϕ', which are the POD modes with matching q, k_z, and k_θ, from two different flows or configurations. For modes from different PODs, the inner product $\langle \phi, \phi' \rangle$ is in general a complex number. For simplicity of analysis, a real number can be defined as the angle θ between the two modes, as

$$\cos\theta = \frac{\Re(\langle \phi, \phi' \rangle)}{\sqrt{\langle \phi, \phi \rangle \langle \phi', \phi' \rangle}},$$

where $\Re$ denotes the real part. This is simply the generalization of the angle between two vectors in the real space using their dot product.

The computed angle $\theta \in [0, \pi]$ quantifies the difference between modes ϕ and ϕ' (closely related to the correlation coefficient) with values close to 0 obtained for similar radial shapes, values close to $\pi/2$ for modes that are completely dissimilar, and values close to π for similar modes where one is the opposite of the other (i.e., negatively correlated, similar to two vectors pointing in opposite directions). Since POD is completely insensitive to the sign of the mode, $\theta = 0$ and π must be interpreted the same way. Therefore, we further map the angle θ onto the interval $[0, \pi/2]$, using the following:

$$\gamma = \frac{\pi}{2} - \left| \theta - \frac{\pi}{2} \right| \in [0, \pi/2].$$

Finally, note that for complex matrices, eigenvectors and therefore the POD (SVD) modes, are unique only up to a constant $\mathrm{e}^{i\alpha}$, where α is a random phase. Therefore, the computed γ can be strongly affected by the arbitrary value of α. This dependence on the random phase shift is then removed by shifting one of the POD modes in increments of 5° over the range $\alpha \in [0, \pi)$, calculating γ for each shift, and taking the minimum value. An example of the impact of this random phase shift on γ, before and after correction, is shown in Figure 4, for the same realization of the flow (same set of snapshots) but different sampling frequencies. Note that both panels show the same comparison, with the only difference being that in one γ is reported without minimization over α and in one it is shown after this corrective step. Since the spatial POD modes are robust to temporal aliasing, we expect values of γ close to 0°, over the majority of streamwise and azimuthal wavenumbers. This is the observed behavior in Figure 4 (b), only after minimization over all α.

The corrected γ (over all α) is the angular distance in function space between mode shapes, measuring how much the radial structure differs between two flows, independent of sign ambiguity, phase ambiguity and energy magnitude. This is reported in degrees for more intuitive interpretation, such that $\gamma \in [0^\circ, 90^\circ]$. Note that $\gamma = 0^\circ$ signifies effectively the same radial shape of the modes and $\gamma = 90^\circ$ shows two modes that are completely independent from each other.

The difference in energy of the modes, i.e., the dependence on u_τ, is included in the singular values associated with each mode, and γ only depends on the shape of the mode. In the rest of this work, we solely focus on γ.

Establishing a Baseline

The impact of various parameters on the shape of the POD modes, and the dissimilarity γ in particular, has to be assessed. Given that the goal is to compare smooth and rough-walled pipes at matched bulk Reynolds numbers (but slightly different friction Reynolds numbers) a few different factors need to be examined, including (i) the sampling (snapshot) frequency, (ii) flow realization and simulation setup, (iii) Reynolds number, and (iv) the radial extent of the domain r_{max} used in the analysis (including calculation of POD modes).

The effect of sampling frequency is examined in Figure 4 (b). It is observed that, for the first quantum index $q = 1$, while some of the modes with $\lambda_z/R \leq 1$ are affected by the sampling frequency (potentially due to their higher frequency in time), the $\lambda_z/R \geq 1$ region is rather insensitive with $\gamma \leq 5^\circ$. The POD modes for P2000-* are computed with a snapshot frequency of $\Delta t U_b/R = 1$ and are, therefore, expected to be robust in the region $\lambda_z/R \geq 1$.

The effect of flow realization and simulation setup is studied in Figure 5 (a) that compares the POD modes of P550-0 from the current simulation campaign, with that of Yao et al. (2023) & Massaro et al. (2024). Note that the two simulations are completely independent of each other, with different solvers and numerics, different domain lengths ($L_z/R = 8\pi$ here and 10π in Massaro et al. (2024)), different grid resolutions, different initial conditions and transient periods, different snapshot collection span, and different snapshot frequencies Δt. While differences as large as $\gamma \approx 60^\circ$ is observed, for the region $\lambda_z/R \geq 1$ (and $\lambda_\theta/R \geq 0.2$, as will be discussed later) not impacted by sampling frequency, the differences reduce to much lower values of $\gamma < 15^\circ$. Whether these differences arise from the different time spans (i.e., statistical convergence of POD modes) or domain lengths (both of which are expected to affect the largest scales) requires further analysis. Nevertheless, the comparison defines a repeatability criterion and tells us (i) to limit our analysis to the region $\lambda_z/R \geq 1$ (and $\lambda_\theta/R \geq 0.2$), and (ii) that differences lower than 15° may be attributed to external factors, rather than a physical difference between the two flows.

The impact of the Reynolds number on the shape of the POD modes in investigated in Figure 5 (b). While the flows of interest are P2000-0, P2000-10, and P2000-20, all at the same

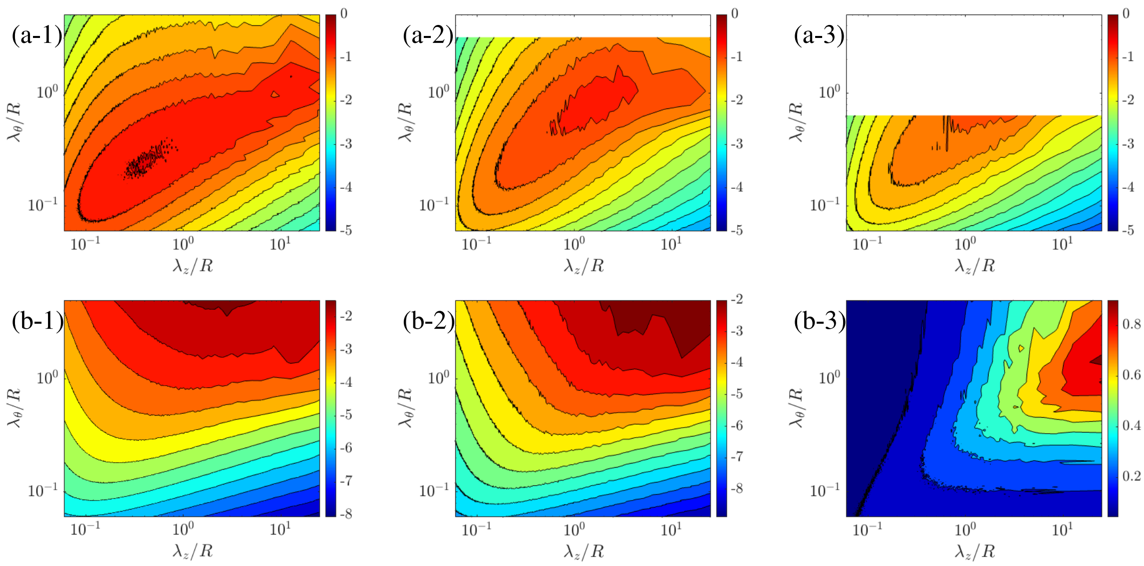

Figure 3: The 2D pre-multiplied energy spectra (in logarithmic scale, base 10) of P2000-0 from the current simulation campaign. Panel (a-1) to (a-3) show $r/R = 0.9$, $r/R = 0.5$, and $r/R = 0.1$, respectively. Panel (b-1) shows the specrum as an integral over circular cross section of the pipe (the mode-by-node total energy as will be decomposed by POD), while panel (b-2) plots the total energy contained in the first POD mode, $q = 1$, only. Panel (b-3) shows the ratio of the energy contained within the $q = 1$ mode compared to the total (ratio of b-2 to b-1) in linear scale. All spectra are normalized by friction velocity. The total energy per mode is the result of a surface integral and is further normalized by the cross section.

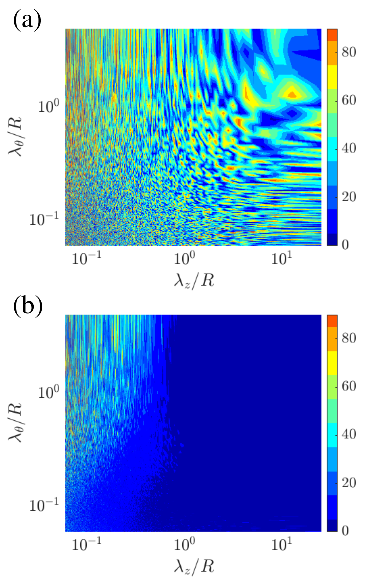

Figure 4: Computed γ (in degrees) for P550-0 comparing POD modes for different snapshot frequencies of $\Delta t U_b/R = 0.5$ and 2: (a) before minimizing γ over incremental phase shifts, and (b) after minimization.

bulk Reynolds number, their observed Re_τ exhibits around 20% difference from one another (Table 1), requiring such assessment. As mentioned earlier, the scaling with friction velocity of the energy of the flow, and therefore the modes, is absorbed into their corresponding energy and the spatial POD modes should be independent of that scaling (for large Reynolds numbers). Despite the rather large difference between the friction Reynolds number of $Re_\tau \approx 1000$ and 2000 for the comparison in Figure 5 (b), it is observed that in the region of interest, $\lambda_z/R \geq 1$ (and $\lambda_\theta/R \geq 0.2$), γ remains within the acceptable threshold of around 15°.

The effect of the radial extent of the domain, r_{max}, is also considered. Figure 2 shows that outer-layer similarity can only be expected sufficiently far from the wall, where the velocity and Reynolds stress profiles become independent of streamwise and azimuthal location along the sinusoidal roughness pattern. The velocity profile of P2000-10 becomes independent of the location for $y^+ \geq 30$, while this occurs around y^+ of 100 for P2000-20. Similarly, Reynolds stresses become independent of location at $y^+ \geq 50$ and 150, respectively. These correspond to $r/R \approx 0.98$ in P2000-10 and 0.95 in P2000-20. The selection of the radial extent is important because (i) the spatial POD modes contain information from the entire domain, (ii) they will change with any change in domain selection, and (iii) the Fourier expansion used here is only valid in the presence of continuous translational symmetry. The effect of r_{max} is studied in Figure 5 (c) and (d), where it is observed that changing r_{max} primarily impacts the region $\lambda_\theta/R \leq 0.2$. The impact is very similar in both P2000-0 and P2000-10 and for r_{max}/R changes from 1.0 to 0.95 and from 0.95 to 0.9 (albeit with some minor differences as well). Importantly, γ remains below 15° in the region of interest: $\lambda_z/R \geq 1$ and $\lambda_\theta/R \geq 0.2$. In the remainder of this analysis, we use $r_{max}/R = 0.90$ for all three cases (P2000-0, P2000-10, and P2000-20), which is well within the acceptable region $r_{max}/R \leq 0.95$ based on Figure 2.

OUTER LAYER SIMILARITY VIA POD

We now examine the outer-layer similarity of the flow. Based on the observations of the previous section, we note that while some variation between POD modes is always expected, in the identified region of interest ($\lambda_z/R \geq 1$ and $\lambda_\theta/R \geq 0.2$), γ remained below 15°. Therefore, values of $\gamma > 15°$ exceeding

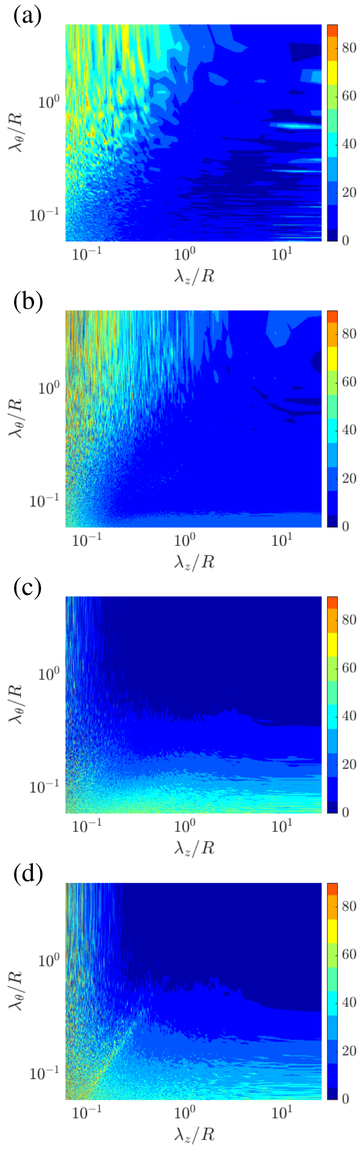

Figure 5: Difference between the radial shape of the $q = 1$ POD modes characterized using γ. Different panels correspond to: (a) the impact of realization, simulation setup, and domain size for P550-0, (b) the impact of Reynolds number for P1000-0 versus P2000-0, (c) the impact of radial extent of the domain included in POD computation (r_{max}) in P2000-0 for $r_{max}/R = 1$ compared to $r_{max}/R = 0.95$, and (d) the same for P2000-10 for $r_{max}/R = 0.95$ compared to $r_{max}/R = 0.9$.

the established threshold could indicate physical differences between the flows beyond computational variability.

Figure 6 presents the main result of this work and compares the shape of the POD modes between P2000-0, P2000-10, and P2000-20. Panels (a) and (b) show that γ for both rough pipes (P2000-10 and P2000-20), when compared to the smooth pipe (P2000-0), rises above the 15° threshold across nearly the entire wavenumber space, except for a narrow region with $\lambda_z/R \geq 4\pi$ ($\lambda_z = L_z/2$) and $\pi/2 \leq \lambda_\theta/R \leq \pi$ ($\lambda_\theta = L_\theta/4$ to $L_\theta/2$). However, the most striking observation is the remarkable similarity between the two rough cases (Figure 6 (c)), where γ values are consistent with those expected from Reynolds number variations alone (cf. Figure 5 (b)). This could suggest an underlying physical difference in the flow

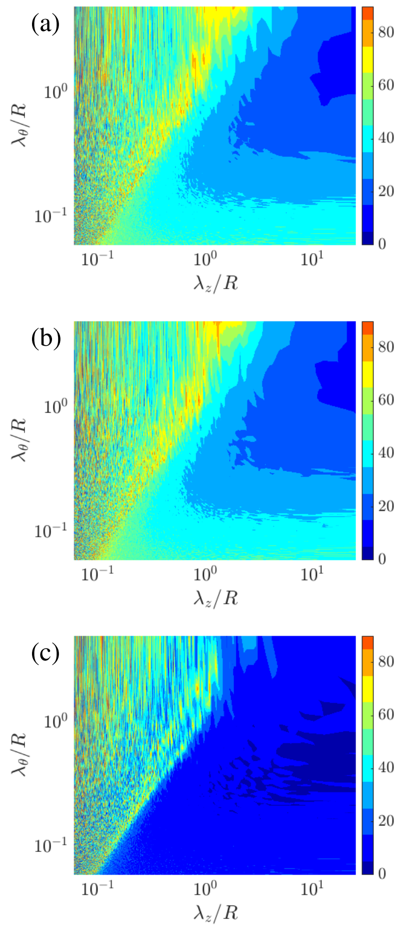

Figure 6: Difference between the radial shape of POD modes characterized using γ: (a) P2000-10 compared to P2000-0, (b) P2000-20 compared to P2000-0, and (c) P2000-10 compared to P2000-20. All panels show the $q = 1$ mode for a domain limited to $r_{max}/R = 0.9$ (for both rough cases as well as the smooth one). The figure shows that modes from different rough cases are more similar to each other (panel (c)), i.e., $\gamma \leq 15°$ in the region $\lambda_z/R \geq 1$ and $\lambda_\theta/R \geq 0.2$, than they are to the smooth-walled modes (panels (a) and (b)).

structure between smooth and rough pipes.

Figure 6 was obtained for $r_{max}/R = 0.9$, but the same qualitative behavior is observed for other r_{max} values of $0.85R$, $0.95R$, and R_{max} (the radius of the roughness peaks). The nearly identical values of γ, especially for $r_{max}/R = 0.85$, indicate that the observed differences are not an artifact of the choice of r_{max}. This suggests that, at this Reynolds number, roughness effects on the flow structure extend beyond $y^+ \approx 300$. An important question for future work is whether there exists a value of r_{max} below which the shape differences between smooth and rough modes vanish, and how such a threshold would scale with Re_τ.

Another interesting observation is the oblique line characterized by $\lambda_\theta \approx \beta \lambda_z^{1.25}$ (for a constant β) where γ jumps to a values above 55°. This is evident in Figure 6 (a) and (b), with a smooth transition toward these higher γ values, but is less pronounced in Figure 6 (c). This region is independent of r_{max}. Comparing with Figure 4 (b) and Figure 5 (a), (b), and (d), several factors (snapshot frequency, flow realization, and Reynolds number) could potentially affect this region. However, the magnitude of γ along this oblique line exceeds what would be expected from such computational sensitivities, as evidenced by the near absence of this feature in Figure 6 (c). While this oblique region may provide further evidence of physical differences between smooth and rough pipe turbulence, detailed analysis is left for future work.

SUMMARY AND CONCLUSIONS

The present work investigates outer-layer similarity in turbulent pipe flows via proper orthogonal decomposition (POD). Multiple factors motivated this choice. POD provides a unified framework that captures spatial correlations across the entire radial domain, ranks flow structures by their energy content, and enables quantitative comparison of flow structures.

The physical motivation for using POD stems from findings of the attached eddy model (AEM; cf. Marusic and Monty, 2019), which suggests that the same logarithmic behavior and scaling laws can be obtained independent of the shape of the attached eddies. Conversely, this finding implies that universal behavior of mean quantities (such as mean velocity and Reynolds stresses) may not necessarily imply universal turbulence structure from a structural perspective; the shape of flow structures can change while exhibiting the same mean profiles. Furthermore, if we accept the AEM and assume that the presence of roughness can change the shape of the attached eddies (over the entire or a large portion of the hierarchy), then the effect of roughness can progress through the entire logarithmic region (or at least a portion of it) and can impact the outer flow at high Reynolds numbers (and potentially all Reynolds numbers, since the logarithmic region also grows). While we did not directly employ the AEM (or other model-based coherent structures), this reasoning was the main motivation why we primarily focused on the difference in the spatial (radial) shape of the POD modes between the rough and smooth pipe flows. Additionally, observations by Ciola et al. (2025) and Maeyama and Kawai (2023) that by removing the near wall region one could get a completely different outer layer go in the same direction and further motivated the focus on outer-layer similarity.

The analysis conducted here suggests potential structural differences in outer-layer turbulence between smooth and rough pipes. This is indicated by the angle between corresponding POD modes rising above a threshold below which differences could be attributed to computational parameters. Further support for this observation is provided by the similarity between the two rough pipes. The present study did not address the cause of these differences, but rather provided evidence that structural differences *may* exist. These findings should guide further investigation aimed at understanding the physical nature of these differences before definitive claims can be made.

Note that the present study focused on the flow through pipes, which is more significantly impacted by the constriction effects from the roughness, such that the mean velocity in the outer-layer (e.g., at the centerline) increases dramatically. Therefore, repeating this study for the turbulent channel flow, or better yet, temporal boundary layers with fixed boundary layer thickness, could help distinguish these constriction effects from the observed structural differences. Similarly, analysis of different friction Reynolds numbers is essential in understanding the dependence of our observations on finite Reynolds number effects.

Finally, this work focused exclusively on *quantifying differences* between POD mode shapes. Several important questions remain for future investigation: (i) the specific mode shapes in smooth and rough pipes, (ii) the physical structures these modes represent, and (iii) the physical mechanisms and implications of shape changes.

REFERENCES

Chan, L., MacDonald, M., Chung, D., Hutchins, N., and Ooi, A., 2018, “Secondary motion in turbulent pipe flow with three-dimensional roughness”, J. Fluid Mech., Vol. 854, pp. 5–33.

Ciola, N., Duguet, Y., Robinet J., De Palma, P., and Cherubini, S., 2025, “Large-scale streak instabilities of transitional channel flow”, J. Fluid Mech., Vol. 1025, pp. A45.

George W. K., 1988, “Insight into the dynamics of coherent structures from a proper orthogonal decomposition”, International Seminar on Wall Turbulence, Dubrovnik, Croatia.

Jansson, N., Karp, M., Podobas, A., Markidis, S., and Schlatter, P., 2024, “Neko: A modern, portable, and scalable framework for high-fidelity computational fluid dynamics”, Comput. Fluids, Vol. 275, pp. 106243.

Maeyama, H., Kawai, S., 2023, “Near-wall numerical coherent structures and turbulence generation in wall-modelled large-eddy simulation”, J. Fluid Mech., Vol. 969, pp. A29.

Marensi, E., Yalnız, G., Hof, B., and Budanur, N. B., 2023, “Symmetry-reduced dynamic mode decomposition of near-wall turbulence”, J. Fluid Mech., Vol. 954, pp. A10.

Marusic, I., and Monty, J., 2019, “Attached Eddy Model of Wall Turbulence”, Annual Rev. Fluid Mech., Vol. 51, pp. 49–74.

Massaro, D., Yao, J., Rezaeiravesh, S., Hussain, F., and Schlatter, P., 2024, “Energy-based characterisation of large-scale coherent structures in turbulent pipe flows”, J. Fluid Mech., Vol. 996, pp. A45.

Rowley C. W., and Marsden, J. E., 2000, “Reconstruction equations and the Karhunen–Loève expansion for systems with symmetry”, Physica D, Vol. 142, pp. 1–19.

Yao, J., Rezaeiravesh, S., Schlatter, P., and Hussain, F., 2023, “Direct numerical simulations of turbulent pipe flow up to $Re_\tau \approx 5200$”, J. Fluid Mech., Vol. 956, pp. A18.